water

MDPI

*Article*

# Spatial-Temporal Variations and Severity of the 2020 Catastrophic Floods in the Yangtze River Basin from Sentinel-1 SAR Data

**Minmin Huang [1,*], Ying Wang [1], Shuanggen Jin [2,3] and Qingxiang Chen [1]**

[1] School of Geographic Information and Tourism, Chuzhou University, Chuzhou 239000, China; vinviyo@foxmail.com (Y.W.); chenqxprime@foxmail.com (Q.C.)
[2] Shanghai Astronomical Observatory, Chinese Academy of Sciences, Shanghai 200030, China; sgjin@shao.ac.cn
[3] School of Surveying and Land Information Engineering, Henan Polytechnic University, Jiaozuo 454003, China
* Correspondence: elffishhmm@foxmail.com

**Abstract:** Flood is one of the most frequent natural disasters in the Yangtze River Basin. Flood risk evaluation is of great social significance, especially for large hydrological systems. Rainfall is both temporal and spatial, influencing surface hydrological activities. The water body range is the final outcome of a flood and can be observed from synthetic aperture radar (SAR) images under any weather condition. A flood severity evaluation model is proposed to quantitatively evaluate the flood based on water body range from area disparity and flood duration. Large hydrological objects usually span a wide range and have significant differences. This results in different initial water areas in each region. This approach addresses the issue through normalization processing. In this paper, Sentinel-1 data are used to extract the temporal water body using the adaptive bimodal method, and the water level data were also incorporated to improve the observation frequency for water area. The flood severity evaluation approach can be used to assess flood risk between any region of large hydrological systems or any flood event, regardless of their regional spatial differences and rainfall duration differences. The results show that: (1) In general, the average water body area in 2020 was 20.40% larger than it was in 2019, and the daily water body areas in 2020 were all greater than the average of 2019 with 71.36% of the days in 2020 having an area greater than the maximum in 2019. The flood severity in 2020 was 1.75 times as much as that of 2019; (2) Reach performance indexes in 2020 were in order of Yueyang (2.21) > Jiujiang (2.04) > Hankou (1.44) > Chizhou (1.32), which were inconsistent with the spatial site; (3) Flood event impact indexes in 2020 were in order as No.2 (1.64) > No.3 (1.61) > No.1 (1.44) > No.4 (1.17) > No.5 (1.15); (4) The flood was more likely the result of cumulative rainfall for 30 days.

**Keywords:** Sentinel-1; water body; flood severity evaluation; flood duration

**Citation:** Huang, M.; Wang, Y.; Jin, S.; Chen, Q. Spatial-Temporal Variations and Severity of the 2020 Catastrophic Floods in the Yangtze River Basin from Sentinel-1 SAR Data. *Water* **2024**, *16*, 3445. https://doi.org/10.3390/w16233445

Academic Editors: Luca Cozzolino, Gaetano Crispino and Oz Sahin

Received: 21 August 2024
Revised: 23 November 2024
Accepted: 27 November 2024
Published: 29 November 2024



## 1. Introduction

Flooding is one of the most destructive and devastating natural disasters. Flood risk evaluation is a crucial approach for disaster prevention and reduction, with great social significance. The Yangtze River (YZR) is the longest river in China and the third longest river worldwide [1] whose water level and water area vary seasonally. The Yangtze River Basin (YZRB) has experienced many severe floods throughout history [2], especially several catastrophic floods [3]. From July 2020 to August 2020, several floods of varying severity affected some reaches of the Yangtze River.

Flood risk evaluation is an easy and intuitive tool for qualifying hazard risk. Three categories of risk analysis approaches have been identified: (1) Mathematical Statistics

Methods, which implement flood evaluation by using historical statistical data [4]; (2) Indicator System Methods, where indicator selection is the core, such as analytical hierarchical process (AHP) [5] and machine learning algorithms [6]; (3) Scenario simulation methods, e.g., using hydrodynamic software to simulate flood features [7–9]. These methods have been successfully employed in flood risk evaluation in the YZRB. Lu et al. [10] proposed a framework for flood risk mapping and influence analysis using hydrodynamic simulations. Sun et al. [2] established a flood disaster risk evaluation model and used three Multi-Criteria Decision-Making (MCDM) methods to compare the flood disaster risk in four administrative units of the Yangtze River Delta. Almost all the flood risk evaluation studies took the land as the target area and the administrative region as the evaluation unit. A large hydrological system is looked at as a whole but usually spans a wide range with significant hydrological differences between different regions, and floods are not confined to simple administrative regions. The flood risk evaluation is usually implemented for rainfall, which does not consider the redistribution of rainfall caused by surface hydrological activities. In addition, flood risk evaluation usually considers flood severity more from the perspective of social impact, such as the potential for loss of life, injury, destruction, or damage to assets. However, for large hydrological systems such as the Yangtze River and the Yellow River, the flood severity reflected by their hydrological states are as important as their direct social impact. In addition, flooding is a complex process, and the hydrological responses to different flood events in different reaches vary greatly. Therefore, a more comprehensive approach to evaluate the flood severity of large hydrological systems between different regions and events is vital, but currently there is a lack of relevant approaches. Water level data and water area data are two factors that can reveal the hydrological status of rivers, which can be considered the final flood results. Although daily water level data provide high temporal resolution, they often offer limited insight since they are single-point measurements. The water area can typically be extracted from satellite images, which can reveal the spatial variation in rivers, but there is a limitation due to the low temporal resolution [11]. Water level and water area usually have a high correlation; therefore, the daily water area data can be estimated by combing water level measures with satellite-derived water area data. A flood severity evaluation approach based on spatial-temporal variations in water body is proposed in this paper, which aims to reveal the risk differences caused by different flood events and quantitatively evaluate the performance of any area with large hydrological systems. The approach focuses on solving the problems caused by inconsistent flood evaluation standards in different regions due to the differences in spatial characteristics and differences in duration of each flood event.

Flood mapping is a critical part of flood severity evaluation. Satellite remote sensing technology can extract large-scale and multi-temporal water area data. With the development of remote sensing technology, the available data sources have increased greatly. Optical satellite images have been widely used for flood mapping for a long time [12,13], but it is difficult to achieve uninterrupted monitoring during flood events due to its vulnerability to cloud cover [14–16]. Satellite synthetic aperture radar (SAR) systems have become the preferred tool for flood mapping [17], owing this to their all-time and all-weather acquisition capabilities. SAR-based water body extraction takes advantage of the unique characteristics of open water in the microwave spectrum [18]. Both supervised and unsupervised methods were employed for flood mapping using SAR images. Image classification or recognition algorithms such as support vector machine (SVM) [19], random forest (RF) [20], and artificial neural networks [21] were used to extract flood extent. Supervised classifications require high-quality training data, which can be difficult to obtain. Unsupervised methods such as histogram thresholding [22], fuzzy c-means clustering, fuzzy decision, and active contour modeling [23] are generalized to image classification or segmentation algorithms. In terms of goals, image segmentation is similar to image classification. Water extraction is usually carried out by image segmentation based on the threshold method [24] which only considers completely inundated areas, such as open water

bodies, to be flooded areas [25], and extracts floods by detecting changes in pre-flood and flooding period. A single threshold is used to separate the open water area and non-water area. Yet, some areas do not become open water even though they were flooded; however, they are not non-water either, like farmlands, for example, that do not become completely covered by the floods [26]. As such, multi-threshold methods were developed to extract the floods from specific objects that were not completely inundated [27].

Sentinel-1 SAR has a high spatial and temporal resolution which can be used to generate the time series of flood maps. The adaptive bimodal method was employed for large-scale water extraction. In this paper, Sentinel-1 GRD images and the adaptive bimodal method are used to obtain the multi-temporal water body area. To obtain the flood duration information, the daily water area was calculated based on the correlation between water level and area. A novel flood severity evaluation approach is proposed to numerically evaluate the flood process from the perspectives of water area disparity and flood duration. The evaluation unit of the novel model is the river reach. The objectives for the study are (1) obtaining the flood spatial-temporal variations during flood season in 2020, (2) quantitatively analyzing the performance for each reach during five flood events in 2020 and evaluating the overall flood severity in 2020.

## 2. Materials and Methods

### *2.1. Study Area*

The YZR can be divided into three streams: the upper stream (above Yichang), the middle stream (from Yichang to Hukou), and the lower stream (from Hukou to the estuary). The water body in the upper stream of the YZR does not change significantly. The middle and lower stream reaches of the YZRB frequently experience heavy rainfall. In particular, the middle stream suffers from floods during the flood season nearly every year [28]. July to August is the flood season in the YZRB.

Catastrophic floods occurred in the middle and lower streams of the Yangtze River in 2020. As such, this paper aims to assess the flood severity in the middle and lower streams. However, satellite imaging cannot cover the entirety of the middle and lower streams; the four reaches (Yueyang, Hankou, Jiujiang, Chizhou) were instead taken as the target objects (Figure 1). Yueyang and Hankou reaches are in the middle stream while Jiujiang and Chizhou reaches are in the lower stream. The Yueyang reach is in the upper stream of the Dongting Lake entrance, and the Jiujiang reach is in the upper streams of the Poyang Lake entrance. Poyang Lake and Dongting Lake are river-communicating lakes in the YZR. The four river reaches were selected for the following three reasons: (1) Historically, flood events occurred frequently in these river reaches. These reaches in Hunan, Hubei, Anhui, and Jiangxi provinces are more prone to flooding. In addition, there are two river-communicating lakes in the Yueyang reach (Dongting Lake) and Jiujiang Lake (Poyang Lake) which have a greater impact on flooding; (2) The coverage frequency and spatial range of Sentinel-1 satellite images determine the extent of the study area. Sentinel-1A and Sentinel-1B satellites can both cover Yueyang, Hankou, and Jiujiang reaches, but the coverage of the two satellites is not consistent. To obtain a higher time observation frequency, both data from the two satellites were used, so the final coverage area is the common coverage area of the two satellites. In each of three river reaches, one scene of Sentinel-1 image was used for water extraction every day. The Chizhou reach is only covered by Sentinel-1A satellite, and the situation in this reach is complicated. The research area is the area covered by two Sentinel-1 images; (3) The extents of the four reaches are not same because the proportion of each reach in the Sentinel-1 image is different, resulting in different scales in the study area. Yueyang and Hankou reaches occupy about one quarter of the images, and Jiujiang and Chizhou reaches occupy about three quarters of the images. Figure 1b–e are Landsat 8 RGB composite images of each reach.

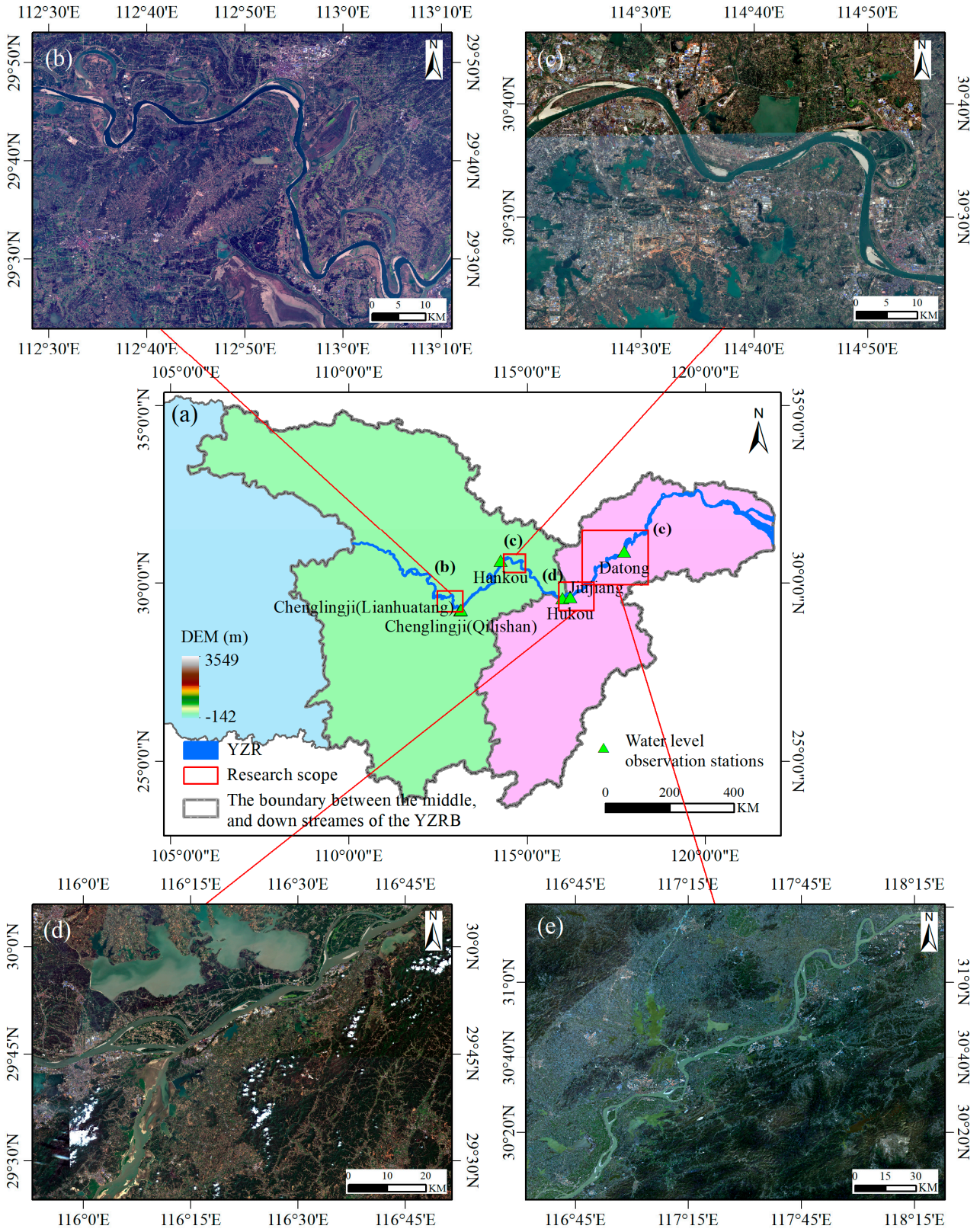


**Figure 1.** Map of the study area: (**a**) the middle and lower streams of YZRB; (**b**) research scope of Yueyang reach; (**c**) research scope of Hankou reach; (**d**) research scope of Jiujiang reach; (**e**) research scope of Chizhou reach.

The floods in 2020 were more severe than those in 2019, with five floods in 2020 and one flood in 2019 during the flood season. The total rainfall recorded by the 39 rainfall

stations in the YZRB from July and August was 17,042.5 mm in 2020 and 11,688.2 mm in 2019, indicating an increase of 45.81%. There were two heavy rainfalls in the middle and lower reaches of the YZR from 3 July to 17 July in 2019, and the flood lasted from 13 July to 17 July in 2019. The total rainfall of the 39 rainfall stations in the YZRB from 3 July to 17 July was 338.69 mm, and the rainfall from 13 July to 17 July was 322.36 mm. While the total rainfall of the 39 rainfall stations in the YZRB from 2 July to 12 July in 2020 was 471.29 mm, which was greater than that of 2019, the rainstorm has continued since 12 July in 2020. It rained almost every day from June to August in the YZRB, and exceptional rainstorms mainly occured from June to mid-July. A brief description of flood events in 2020 is provided in Table 1. The first flood of the YZR in 2020 was largely a result of the previous rainfall in June.

**Table 1.** A brief description of flood events in 2020.

| Flood Events | Date | Duration | Atd_R_2020 [1] | Atd R_2019 [1] | Rainfall Increase |
|---|---|---|---|---|---|
| No.1 | 2 July–12 July | 11 days | 471.29 | 320.5 | 47.05% |
| No.2 | 17 July–22 July | 6 days | 388.5 | 293.17 | 32.52% |
| No.3 | 26 July–29 July | 4 days | 281.4 | 77.95 | 261.00% |
| No.4 | 14 August–16 August | 3 days | 188.17 | 67.2 | 180.01% |
| No.5 | 17 August–After 20 August | >4 days | 335.5 | 63.9 | 425.04% |

Note: [1] Atd_R means the average total daily rainfall of the 39 rainfall stations in the YZRB.

### *2.2. Data Sets*

#### 2.2.1. Sentinel-1 GRD Product

Sentinel-1 provides level 1 ground range detected (GRD) products. GRD products consist of focused SAR data that have undergone multilooking processing and were projected to ground range using an Earth ellipsoid model. GRD products are widely used in studying the backscattering of land cover and monitoring water bodies [23]. Different polarization observation modes of Sentinel-1 show different detection sensitivities to the land surface [29]. GRD products provide amplitude and intensity bands with both Vertical–Horizontal (VH) and Vertical–Vertical (VV) polarization [30,31]. Detailed information of Sentinel-1 GRD products are shown in Table 2. The original spatial resolution of the product is 5 m × 20 m, and the spatial resolution of the preprocessed product can be 10 m × 10 m. Raw Sentinel-1 GRD images can be downloaded from the Alaska Satellite Facility (https://asf.alaska.edu/). Google Earth Engine platform (https://code.earthengine.google.com/) provides the preprocessed Sentinel-1 GRD data collection ("COPERNICUS/S1_GRD").

**Table 2.** Information of Sentinel-1 GRD products.

| Operation Mode | Incident Angle | Spatial Resolution | Image Width | Polarization Mode |
|---|---|---|---|---|
| Interferometric wide swath (IW) | 29~46° | 5 m × 20 m | 250 km | VH + VV |

Table 3 shows the information about Sentinel-1 images covering each reach during flood events in 2019 and 2020. Sentinel-1 GRD products with VH polarization were used to extract the water body, whose spatial resolution is 10 m after preprocessed.

**Table 3.** Information from Sentinel-1 images covered each reach during flood events.

| Year | Reach | Number of Images | Detailed Date of Images |
|---|---|---|---|
| 2020 | Yueyang | 10 | July: 01, 13, 18, 25, 30<br>August: 06, 11, 18, 23, 30 |
| | Jiujiang | 11 | July: 02, 08, 14, 20, 26<br>August: 01, 07, 13, 19, 25, 31 |

| | | | |
|---|---|---|---|
| 2019 | Hankou | 11 | July: 01, 08, 13, 20, 25<br>August: 01, 06, 13, 18, 25, 30 |
| | Chizhou | 10 | July: 03, 15, 27<br>August: 08, 20<br>September: 01 |
| | Yueyang | 10 | June: 30<br>July: 12, 19, 24, 31<br>August: 05, 12, 17, 24, 29 |
| | Jiujiang | 11 | July: 02, 08, 14, 20, 26<br>August: 01, 07, 13, 19, 25, 31 |
| | Hankou | 11 | July: 02, 07, 14, 19, 26, 31<br>August: 07, 12, 19, 24, 31 |
| | Chizhou | 6 | June: 27<br>July: 09, 21,<br>August: 02, 14, 26 |

#### 2.2.2. Planet Images

Optical images were used as true flood maps for validation. During flood events, several Landsat 8 and Sentinel 2 images were available, but only a few of them were consistent with the dates of Sentinel-1 images, as most of them were covered by clouds. To address this limitation, Planet images (https://www.planet.com/explorer/) (accessed on 3 February 2021) were used as validation data. Planet Labs operates a fleet of micro-satellites that provide daily global coverage, making it possible to monitor and capture changes across the entire earth with high observation frequency. It provides four bands: red, green, blue, and NIR. A total of eight Planet images, acquired during flood events, were used to perform the validation; the information is shown in Table 4.

**Table 4.** Information from Planet images.

| Reach | Date | Product |
|---|---|---|
| Wuhan | 1 August 2020<br>(accessed on 3 February 2021) | 20200801_025555_1105<br>20200801_025557_1105 |
| Hukou | 19 August 2020<br>(accessed on 3 February 2021) | 20200819_023612_100a<br>20200819_023613_100a |
| Yueyang | 5 August 2020<br>(accessed on 3 February 2021) | 20200805_025002_1032<br>20200805_025003_1032 |
| | 23 August 2020<br>(accessed on 3 February 2021) | 20200823_024851_103c<br>20200823_024852_103c |

#### 2.2.3. Measured Water Level Data

The measured water level data were downloaded from the website of the Changjiang Maritime Safety Administration (https://cj.msa.gov.cn/). There are 13 hydrological stations in the YZR, and 6 stations among them are located within or close to the study area of this paper. Chenglingji (Lianhuatang) and Chenglingji (Qilishan) stations are close to the Yueyang reach, Hankou stationis located within the Hankou reach, Jiujiang and Hukou stationsare located within the Jiujiang reach, and Datong Station is located within the Chizhou reach.

#### 2.2.4. Rainfall Data

The brief description of the flood events in 2020 (Section 2.1) was based on rainfall station data which compared rainfall in the YRB during the flood season of 2020 with that of 2019. The rainfall data were downloaded from the website of the China Meteorological

Data Service Center (http://data.cma.cn/). Its data format is txt. There were 39 global rainfall observation stations in the YZRB.

The spatial-temporal variations in rainfall in 2020 (Section 3.1) were derived from the NASA Global Precipitation Measurement (GPM) Integrated Multi-Satellite Retrievals for GPM (IMERG) Final Precipitation Level 3 V06. The rainfall data collection can be downloaded from https://disc.gsfc.nasa.gov/. The IMERG is a NASA product estimating global surface precipitation rates at a high resolution of 0.1° every half-hour beginning 2000. The IMERG Final Precipitation represents the final estimate of the daily mean precipitation rate in mm/day. The spatial resolution of the data set is 0.1 degree × 0.1 degree. Its original data format is netCDF, and the data are finally processed into tif images.

### *2.3. Methods*

Multi-temporal Sentinel-1 images were used to extract the water area during 5 flood events in 2020. Daily water area was calculated through regression analysis of water area and water level. A novel flood severity evaluation approach is proposed to numerically evaluate the impact of each flood event and the performance for each reach. Four indicators were selected to evaluate flood risk from the perspectives of water area disparity and flood duration. The analytic hierarchy process (AHP) method was applied to assign the weight of each indicator. The evaluation unit is defined as the river reach. The hydrological and topographical conditions of each river reach are different, and evaluation based on the absolute water area can lead to inconsistent reference standards for each river reach. Therefore, this approach ensures that the standards for risk evaluation are consistent by normalization based on the historical water area of each river reach. This approach can be used to assess flood risk between any region of large hydrological systems or any flood event, regardless of their regional spatial differences and rainfall duration differences. A flow chart detailing the flood analysis methodology used in this study is shown in Figure 2.

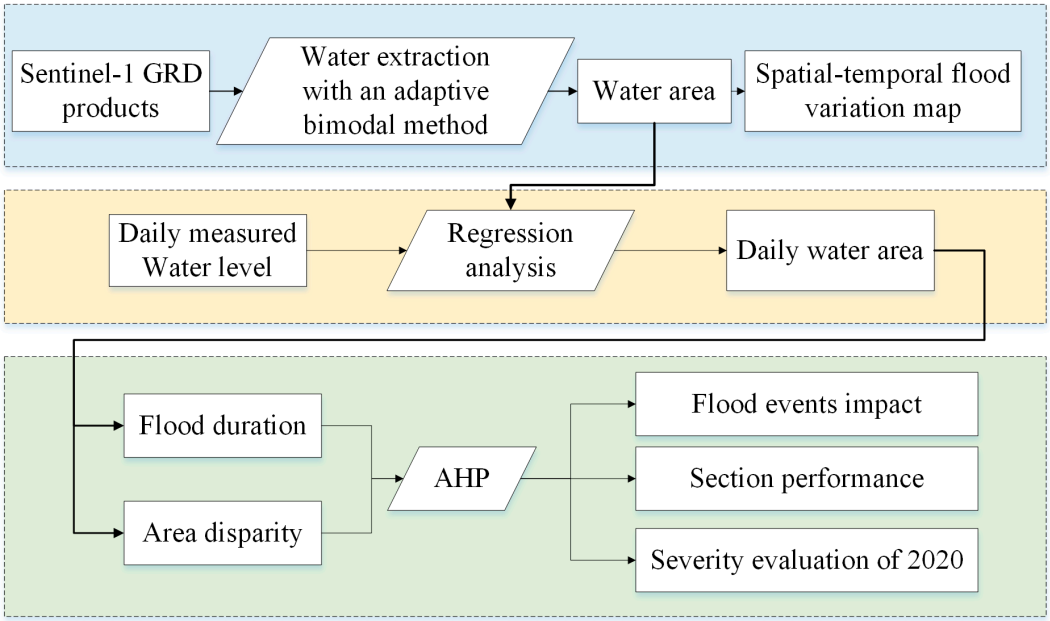


**Figure 2.** Flow chart of water extraction and flood evaluation.

#### 2.3.1. Sentinel-1 GRD Data Processing

The pre-processing of the SAR data involves orbit correction, radiometric calibration, speckle filtering, multilooking, and geometric correction. For Sentinel-1 data, orbit correction is generally divided into coarse and fine orbit correction. The coarse orbit information is included in the metadata of SAR products, with an accuracy of within 10 cm.

The precise orbit file is usually published on the official orbit website 21 days after the product is generated. The precise orbit file provides accurate satellite position and velocity information, and its position accuracy is within 5 cm. Radiometric calibration establishes a precise relationship between the SAR image and ground object backscatter, which allows the simple conversion of image intensity value to Sigma or Gamma. Speckle filtering is applied to reduce image noise. Multilooking processing averages the range and azimuth resolutions of the image to suppress speckle noise which reduces spatial resolution but enhances radiometric resolution. Geometric correction is performed to accurately position the image on the Earth (geocoding) and to correct terrain distortions caused by terrain variations and sensor geometry [17].

#### 2.3.2. Water Extraction Methods

The histogram bimodal method is a classic method used for binary image segmentation. Its fundamental principle is that when the histogram of an image has typical bimodal features, the pixel value of the lowest point between the two peaks is the segmentation threshold. In SAR imagery, water bodies typically exhibit specular reflection, resulting in low scattering coefficients. Consequently, all pixels on the image with values less than the segmentation threshold are classified as water bodies. Due to the unique characteristics of water bodies in SAR images, this method can effectively distinguish water bodies from other land types. Despite its simplicity and convenience, the histogram bimodal method requires an appropriate ratio of target pixels and background pixels on the image. For effective water body extraction using SAR images, it is necessary to adjust the range of the image so that the distribution histograms of water body pixels and background pixels conform to a bimodal distribution. In this paper, the image area was manually adjusted to achieve a superior bimodal histogram. Figure 3 provides an example. Figure 3a shows the adjusted image range of the Hankou reach to produce a well-defined bimodal distribution histogram. Figure 3b shows the histogram distribution of the image with an excellent bimodal distribution where the horizontal axis represents the pixel value, and the vertical axis represents the pixel density (or ratio).

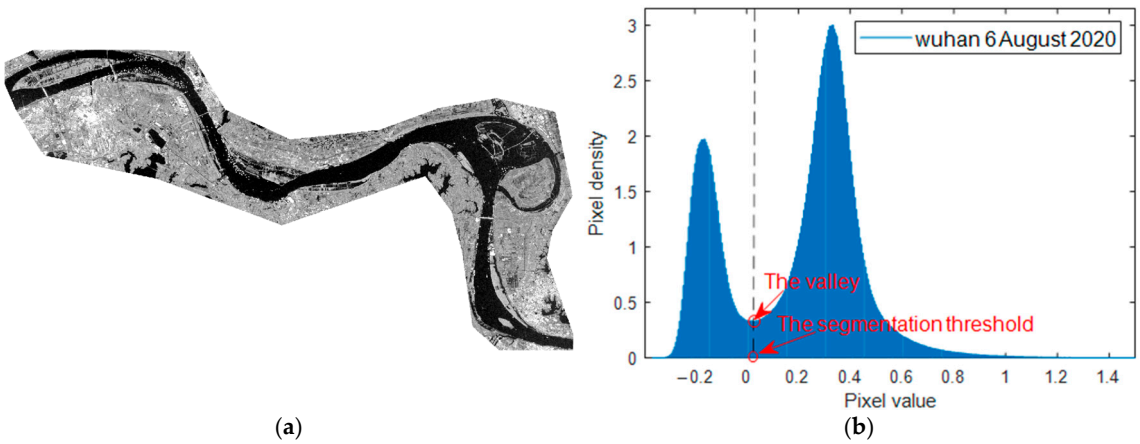


(**a**) (**b**)

**Figure 3.** (**a**) Sentinel-1 GRD image of VH polarization in Wuhan on 6 August 2020; (**b**) Histogram of the image indicating the threshold to retrieve water body.

Water extraction from optical images is commonly performed using *the normalized difference water index (NDWI)* in (1) [32]. A threshold is applied to segment the water index image into a binary water map to obtain the water area.

$$NDWI = (\rho_{Green} - \rho_{NIR})/(\rho_{Green} + \rho_{NIR}), \quad (1)$$

where $\rho_{Green}$ means the reflectance of *the green band*, and $\rho_{NIR}$ means the reflectance of *the near-infrared (NIR) band*.

2.3.3. A Flood Severity Evaluation Approach

The Process of the Flood Severity Evaluation Approach

The flood severity evaluation approach aims to reveal the risk differences caused by different flood events and quantitatively evaluate the performance for each reach. Thus, it generates three results: flood event impact index, reach performance in flood, and composite flood severity index. *Flood event impact index (FI)* measures the severity difference caused by each flood event. Its purpose is to quantitatively evaluate the differences in impact between five flood events. The evaluation object is each flood event from the time aspect, while it considers four river reaches as a whole from a spatial aspect. That is, *FI* evaluates the overall flood severity of four reaches in each flood event. *Reach performance index in flood (RP)* quantifies the severity differences in reaches in flood events. Its objective is to quantitatively evaluate the differences in the impact of floods on each river reach in 2020. The evaluation object considers five flood events as a whole from a time aspect while it also refers to each river reach from a spatial aspect. That is, *RP* evaluates the overall impact of all flood events in each reach. *Composite flood severity index (CFSI)* reflects the flood severity of all flood events in all reaches. Its objective is to quantitatively evaluate the flood severity in all river reaches in 2020 compared with those in 2019. The evaluation object takes five events as a whole from a time aspect while it takes four river reaches as a whole from a spatial aspect. Table 5 provides a brief explanation for the three flood risk evaluation indicators, clarifying their significance and roles in the analysis.

**Table 5.** A brief explanation of the three flood risk evaluation indices.

| Evaluation Indices | Time Aspect | Spatial Aspect | Objective |
|---|---|---|---|
| *FI* | Each flood event | Four river reaches as a whole | Quantitatively evaluate the differences in impact between five flood events. |
| *RP* | Five flood events as a whole | Each reach | Quantitatively evaluate the differences in the impact of floods on each river reach in 2020. |
| *CFSI* | Five flood events as a whole | Four river reaches as a whole | Overall evaluation of the flood severity in all river reaches in 2020. |

The main steps of this approach are as follows:

(1) Select several areas of the hydrological system as evaluation objects;
(2) Find the water area when no floods have occurred to act as the benchmark for risk evaluation. Because the hydrological characteristics of large water bodies usually exhibit annual periodic changes, water bodies that have not experienced floods during the same period in previous years can serve as the benchmark;
(3) Use remote sensing or hydrological methods to calculate the water area of each evaluation object on different dates;
(4) Calculate the average and maximum water area of each evaluation object during the same period in previous years;
(5) Calculate the average and maximum water area of each rainstorm event during the flooding period;
(6) Construct the indicator system from the perspectives of water area disparity and flood duration. The secondary evaluation indicators take the water area during the same period in previous years of the same region as a benchmark to eliminate differences in the area and space of different evaluation objects;
(7) Determine the weight of each indicator;
(8) Calculate the index values of a single rainstorm event of each evaluation object according to step (6). Divide an index value by the sum of the index values of all evaluation objects during the rainstorm event to obtain the normalized index value. The normalized index value can eliminate the influence of rainstorm event time difference.

(9) Calculate *FI*, *RP*, and *CFSI*.

When selecting the evaluation objects (in step (1)), it is unnecessary to consider whether the spatial characteristics of different areas, such as length, width, and area, are consistent. The differences in spatial characteristics are eliminated by taking the water area during non-flood periods as a benchmark (in step (2)). Differences in the days of each flood event are eliminated by calculating the proportion of days related to indicators during each flood period.

Detailed information on indicator selection and quantification, index weight calculation, and flood severity calculation will be explained in the following text.

Indicator Selection and Quantification

The evaluation is conducted from two perspectives: area disparity and flood duration. The two indicators can be further subdivided according to evaluation objects. The detailed indicators are shown in Table 6.

**Table 6.** Severity evaluation indicators.

| First-Level Indicators | Second-Level Indicators | Details |
|---|---|---|
| Water area disparity | I1 [2] | Increase in average area in 2020 compared with that in 2019 |
| | I2 [3] | Increase in max area in 2020 compared with that in 2019 |
| Flood duration | I3 [4] | The proportion of days in 2020 with an area greater than the average of 2019 to the days of each flood event in 2020 |
| | I4 [5] | The proportion of days in 2020 with an area greater than the maximum of 2019 to the days of each flood event in 2020 |

Notes: [2] I1 means the first second-level severity evaluation indicator. [3] I2 means the second second-level severity evaluation indicator. [4] I3 means the third second-level severity evaluation indicator. [5] I4 means the fourth second-level severity evaluation indicator.

The score of indicator 1 in reach *i* in flood event *j* can be calculated as:

$$\mathrm{I1}_{ij} = \frac{area\_20_{ij} - area\_19_i}{Average\_area\_2019_i}, \quad (2)$$

where $area\_20_{ij}$ means the average area of reach *i* in flood event *j* in 2020, and $area\_19_i$ means the average area of reach *i* in 2019.

The score of indicator 2 in reach *i* in flood event *j* can be calculated as:

$$\mathrm{I2}_{ij} = \frac{Marea\_20_{ij} - Marea\_19_i}{Marea\_19_i}, \quad (3)$$

where $Marea\_20_i$ means the max area of reach *i* in flood event *j* in 2020, and $Marea\_19_i$ means the max area of reach *i* in 2019.

The score of indicator 3 in reach *i* in flood event *j* can be calculated as:

$$\mathrm{I3}_{ij} = \frac{Gdays\_20_j}{Tdays\_20_j}, \quad (4)$$

where $Gdays\_20_j$ means days in 2020 with an area greater than the average of 2019 in flood event *j*, and $Tdays\_20_j$ means total flood days in flood event *j* in 2020.

The score of indicator 4 in reach *i* in flood event *j* can be calculated as:

$$\mathrm{I4}_{ij} = \frac{Mdays\_20_j}{Tdays\_20_j}, \quad (5)$$

where $Mdays\_20_j$ means days in 2020 with an area greater than the maximum of 2019 in flood events.

Index Weight Calculation

The analytic hierarchy process (AHP) method is a simple decision-making tool to deal with complex, unstructured, and multi-attribute problems [33,34]. It has been extensively applied in severe natural hazards evaluation like floods and landslides [21]. This model is centered on multi-criteria and multiple objectives, including the contribution of the experts on their expert knowledge and judgment. The weight of each factor was revealed via the following pairwise comparison matrix in Equation (6).

$$A = (a_{ij}) = \begin{bmatrix} 1 & a_{12} & \cdots & a_{1n} \\ 1/a_{12} & 1 & & a_{2n} \\ \vdots & & \ddots & \vdots \\ 1/a_{1n} & 1/a_{2n} & \cdots & 1 \end{bmatrix}, \quad (6)$$

where $A = (a_{ij})$ is a representation of the importance of one factor over another compared to alternative $a_{ij}$ and all comparisons $i, j = 1, 2, \ldots, n$.

The pairwise comparison judgments were carried out by using the nine-point scale. The matrix was constructed by rating the importance of each factor to other factors. The largest eigenvalue and its corresponding eigenvectors were calculated by the matrix, and the corresponding eigenvectors were the importance ranking of each factor, which is also the weight matrix. To reduce the error caused by one-sidedness, a consistency check must be performed by the *consistency ratio* (*CR*) and the *consistency index* (*CI*) value. When the *CR* was equal to or less than 0.1, the calculated weight matrix was acceptable. The *random consistency index* (*RI*) is 0.89 when the number of factors is 4.

$$CI = \frac{\lambda max - n}{n-1}, \quad (7)$$

$$CR = \frac{CI}{RI} \quad (8)$$

where $\lambda max$ is the largest eigenvalue of the pairwise comparison matrix, and $n$ is the number of factors.

Flood Severity Index Calculation

*FI* is used to evaluate the impact of each flood event in 2020 and the computing cells were the four reaches, which can be calculated as:

$$FI_i = \sum_{j=0}^{4}(w_1 \times I1_{ji} + w_2 \times I2_{ji} + w_3 \times I3_{ji} + w_4 \times I4_{ji}), \quad (9)$$

where $i$ means the number of flood events and belongs to 1, 2, 3, 4, 5.

*RP* is used to evaluate the performance for each reach during all flood events in 2020, and the computing cells were the flood events, which can be calculated as:

$$RP_i = \sum_{j=0}^{4}(w_1 \times I1_{ij} + w_2 \times I2_{ij} + w_3 \times I3_{ij} + w_4 \times I4_{ij}), \quad (10)$$

where $i$ means the number of reaches and belongs to 1, 2, 3, 4.

*CFSI* is used to evaluate the flood severity of all flood events in all reaches, which can be calculated as:

$$CFSI = (\sum_{j=0}^{4} SP_i)/4, \quad (11)$$

## 3. Results and Analysis

### *3.1. Spatial-Temporal Variations in Rainfall in 2020*

To explore the impact of rainfall on floods, this study selected six indicators from two dimensions, rainfall intensity and rainfall duration, to describe the rainfall in each flood event (Table 7). To some extent, rainfall duration can be reflected by the cumulative rainfall in the early stages of flood events. Figure 4 shows the change process of 6 rainfall indicators.

**Table 7.** Rainfall indicators.

| ID | First-Level Indicator | Second-Level Indicator |
|---|---|---|
| 1 | Rainfall intensity | The average daily rainfall during each flood event |
| 2 | | The cumulative rainfall during each flood event |
| 3 | | The maximum daily rainfall during each flood event |
| 4 | Rainfall duration | The cumulative rainfall for 10 days before each flood event |
| 5 | | The cumulative rainfall for 15 days before each flood event |
| 6 | | The cumulative rainfall for 30 days before each flood event |

Among the three rainfall intensity indicators, the intensity of the five floods is constantly weakening. The intensity of the No.1 and No.2 flood events is much greater than that of the following three, especially the intensity of the No.1 flood event.

From the three rainfall duration indicators, there were three main conclusions: (1) Among the five flood events, the three previous cumulative rainfall indicators of the No.2 flood event were all the highest, slightly exceeding that of the No.1 flood event; (2) There is no significant difference in the previous cumulative rainfall indicators of the No.4 and No.5 flood events; (3) From the cumulative rainfall between 10 and 15 days before each flood event, it can be found that the No.1 and No.2 flood events are much more serious than the following three events. With regard to the cumulative rainfall in the 30 days before each flood event, the first three flood events had significantly more rainfall than the latter two.

In terms of the spatial distribution, the rainfall intensity duration indicators exhibit opposing spatial results in the midstream and downstream. From the rainfall intensity indicators, the rainfall in the downstream was greater than that in the midstream; from the rainfall duration indicators, the rainfall in the midstream was generally greater than that in the downstream.

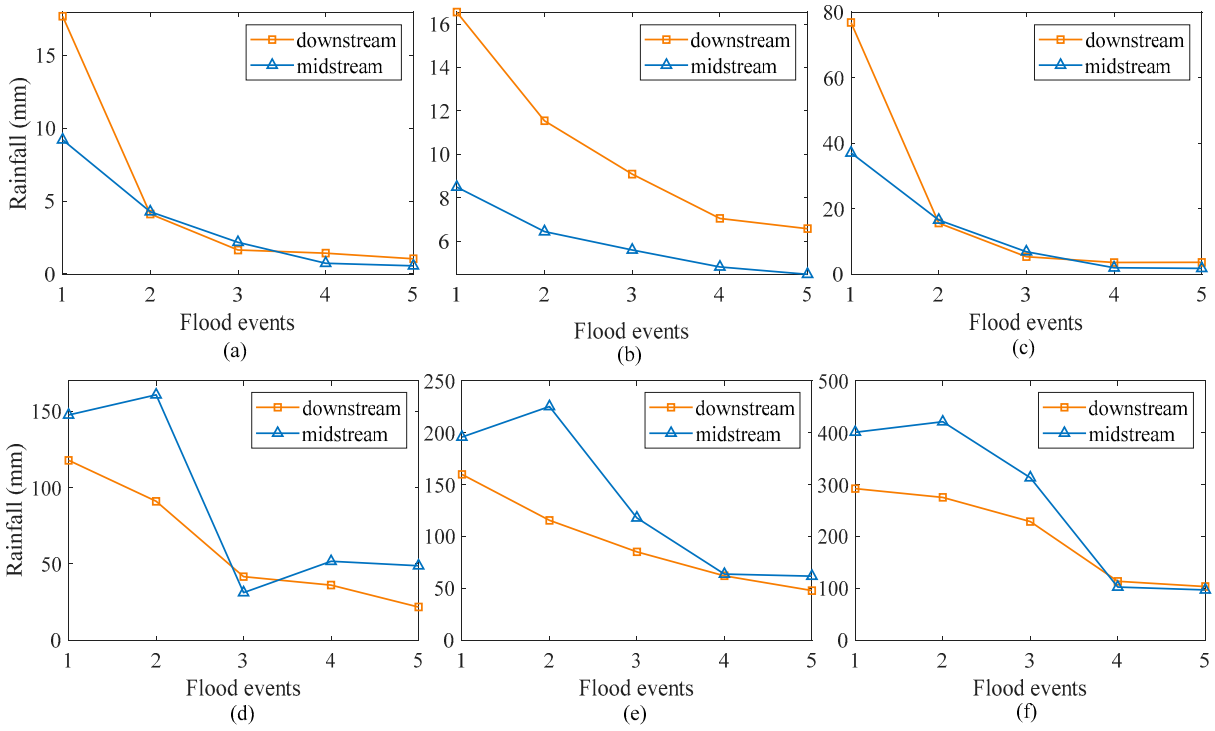


**Figure 4.** The line charts of rainfall during each flood event: (**a**) The average daily rainfall; (**b**) The maximum daily rainfall; (**c**) The cumulative rainfall during each flood event; (**d**) The cumulative rainfall for 10 days before the flood event; (**e**) The cumulative rainfall for 15 days before the flood event; (**f**) The cumulative rainfall for 30 days before the flood event.

### *3.2. Spatial-Temporal Variations in Floods*

#### 3.2.1. SAR-Derived Water Body Validation

The areas of the four reaches on each date were extracted from Sentinel-1 images with the adaptive bimodal method. To validate the accuracy of water body extraction, the water bodies extracted by NDWI from Planet images (Figure 5) were treated as the true flood map. The difference in percentage of water body between the two methods is shown in Table 8. The absolute values of difference percentage were below 10%, except for that of the Yueyang reach on 5 August 2020. The Planet images of the Yueyang reach were on 5 August, while the Sentinel-1 images were on 6 August. The water area on 6 August was less than that of 5 August according to the water level of the two days, so the difference percentage on 6 August should be less than 12.8%. As such, the approach of water body extraction from Sentinel-1 images with the adaptive bimodal method is reasonable and practicable.

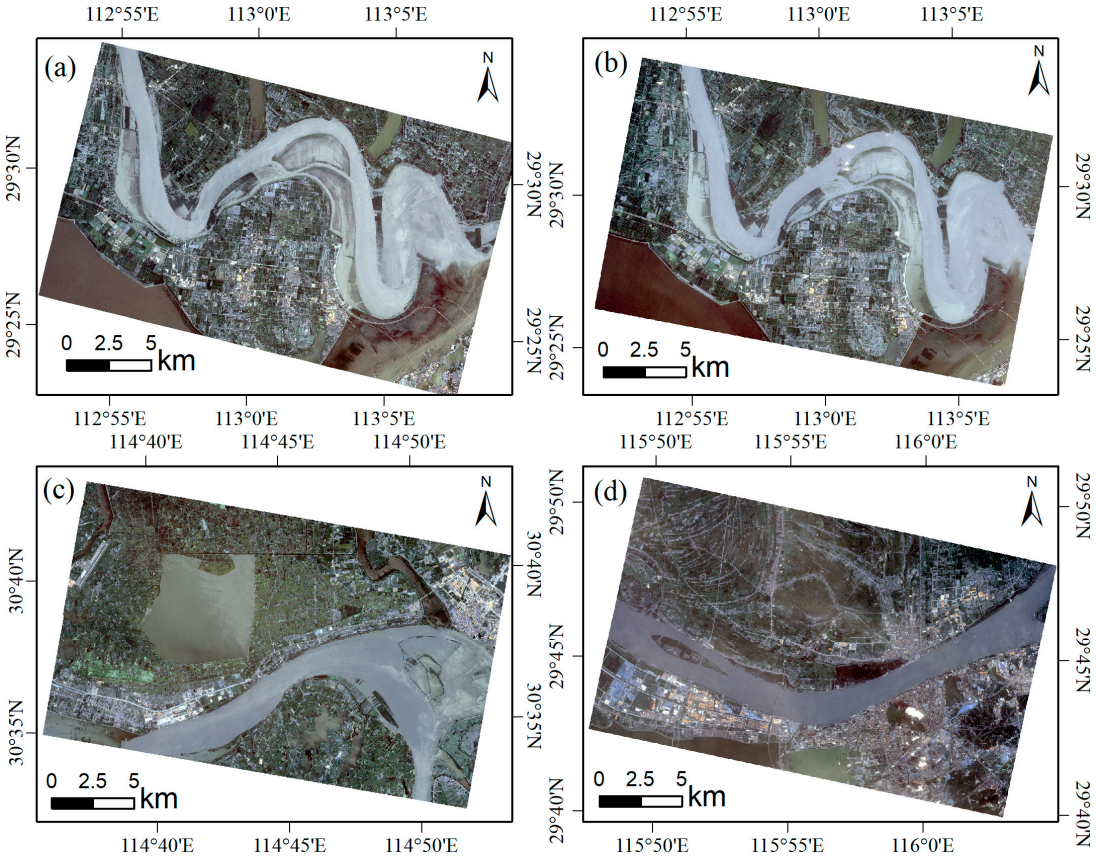


**Figure 5.** Planet images in different reaches: (**a**) Yueyang reach on 5 August 2020; (**b**) Yueyang reach on 23 August 2020; (**c**) Hankou reach on 1 August 2020; (**d**) Jiujiang reach on 19 August 2020.

**Table 8.** Difference in percentage of water area between the two methods.

| Reach | Date | Water Area with SAR (km²) | Date | Water Area with Planet (km²) | Different Percent |
|---|---|---|---|---|---|
| Yueyang | 6 August 2020 | 90.41 | 5 August 2020 | 103.68 | −12.80% |
| Yueyang | 23 August 2020 | 84.94 | 23 August 2020 | 94.25 | −9.87% |
| Hankou | 1 August 2020 | 70.22 | 1 August 2020 | 73.4 | −4.33% |
| Hukou | 19 August 2020 | 53.09 | 19 August 2020 | 57.51 | −7.68% |

#### 3.2.2. Daily Water Area Calculation Based on Correlation Between Water Level and Area

There are two hydrological stations near the Yueyang reach of the YZR: Chenglingji (Lianhuatang) and Chenglingji (Qilishan). Hankou Station is located within the Hankou reach; Jiujiang Station, and Hukou Station are within the Jiujiang reach; and Datong Station is within the Chizhou reach. The R-square values between water level and area of the four reaches and the trend of water level and area is also shown in Table 9. The water area of the four reaches shows a highly positive correlation with the water level, with a maximum value of 0.99 and a minimum value of 0.77.

**Table 9.** Coherence between water level and area.

| Reach | Station | R-Square |
|---|---|---|
| Yueyang | Chenglingji (Lianhuatang) | 0.77 |
| | Chenglingji (Qilishan) | 0.77 |
| Hankou | Hankou | 0.92 |
| Jiujiang | Jiujiang | 0.99 |
| | Hukou | 0.90 |
| Chizhou | Datong | 0.97 |

3.2.3. Spatial-Temporal Variations in Floods in 2020

Table 10 and Figure 6 show the water body changing processes during each flood event in 2020. It can be found that: (1) The areas of the four reaches during five flood events in 2020 were greater than the average area during the flood season (July and August) in 2019; (2) The water body area and its increase curves of the four reaches show a single peak, with the peak occurring during the second or third flood event, and the water area at the beginning of the flood season (No.1 flood event) is greater than the area at the end of the flood season (No.5 flood event); (3) The overall trends of water area and their increase in Hankou, Jiujiang, and Chizhou reaches were consistent, with the peak occurring during the second flood event; the peak of water area in the Yueyang reach occurred during the No.3 flood event; (4) The order of area increase in each flood event is as follows: Yueyang > Jiujiang > Hankou > Chizhou. The average increase in Yueyang and Jiujiang is similar, both at 25% to 30%, while the average increase in Chizhou and Hankou is similar, ranging from 10% to 15%.

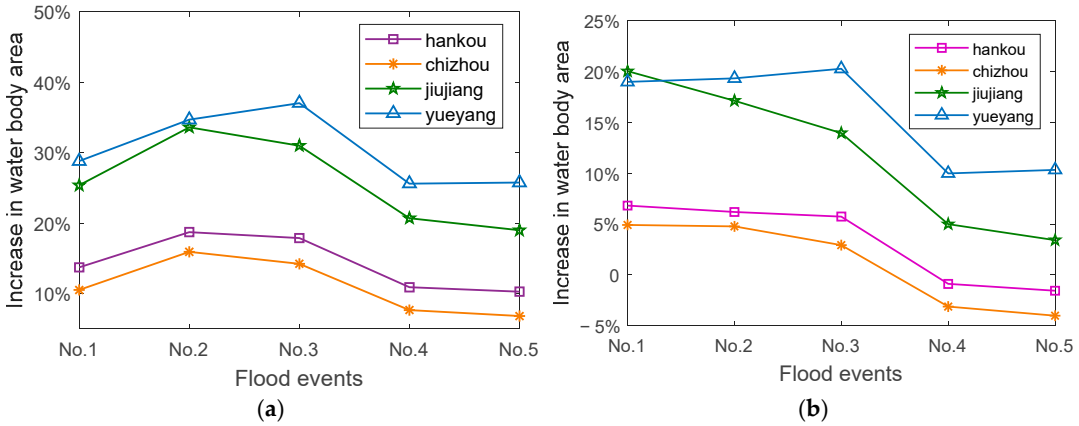


**Figure 6.** (**a**) Increase in average area of each flood event in 2020 compared with the average area during July and August in 2019; (**b**) Increase in max area of each flood event in 2020 compared with the max area during July and August in 2019.

**Table 10.** Increase in average area of each flood event in 2020 compared with the average area during July and August 2019.

| Stream | Reach | No.1 | No.2 | No.3 | No.4 | No.5 | Mean |
|---|---|---|---|---|---|---|---|
| Midstream | Yueyang | 28.79% | 34.68% | 37.02% | 25.60% | 25.75% | 30.37% |
| | Hankou | 13.72% | 18.72% | 17.87% | 10.89% | 10.28% | 14.30% |
| Downstream | Hukou | 10.51% | 15.92% | 14.23% | 7.66% | 6.81% | 11.02% |
| | Chizhou | 25.36% | 33.59% | 30.99% | 20.70% | 18.98% | 25.92% |

Figure 7 shows the inundation map of each reach. With the SAR-derived water area, it can be seen that the water bodies increased rapidly during the first half of July and reached almost its largest size around mid-July during the floods; only the inundation map around mid-July was presented here to reveal the flood's spatial distribution.

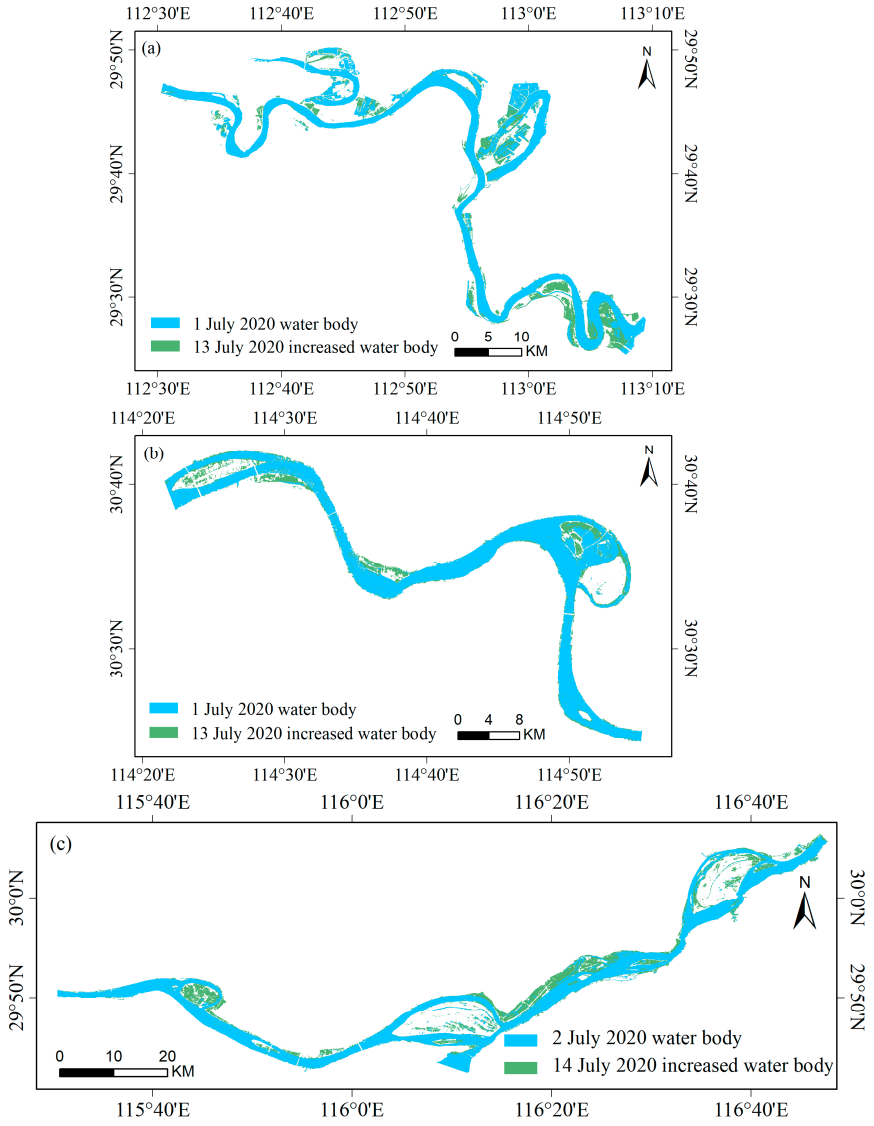

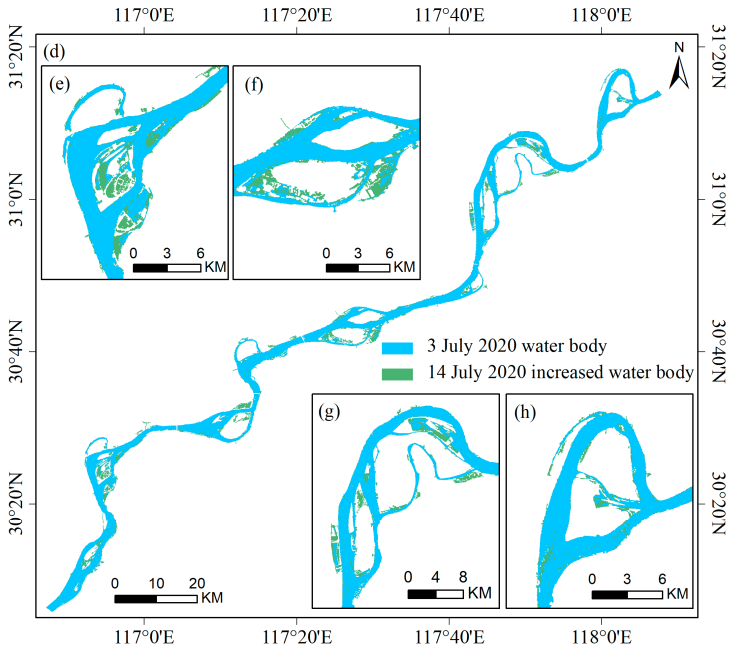


**Figure 7.** The flood map of four reaches: (**a**) Yueyang reach; (**b**) Hankou reach; (**c**) Jiujiang reach; (**d**) Chizhou reach; (**e**–**h**): Local enlarged drawings of Chizhou reach.

### *3.3. Flood Severity Evaluation in 2020*

#### 3.3.1. Flood Severity Index in 2020

The weight matrix was assigned by the AHP method with the value of each index as follows: 0.466, 0.277, 0.161, and 0.096. The *CI* value of this weighting scheme was 0.008728, which is below 0.1 and acceptable, and the *CR* value was 0.009807.

There were five floods in 2020 and one flood in 2019 during the flood season. The flood in 2019 was not serious compared with historical records and was considered a normal state for a YZR flood. The detailed scores for relative flood severity in each reach are shown in Table 11, which means each indicator in the four reaches was used to describe the relative flood severity. Only the SAR-derived results were used to compute in this section. In conclusion, the average water body area in 2020 was 20.40% larger than that in 2019 in the four reaches of the YZR. The max water body area was 16.46% larger than that of 2019. Even the water body areas every day in 2020 were greater than the average of 2019. 71.36% of days in 2020 had an area greater than the maximum of 2019, compared to the total flood days in 2020.

**Table 11.** Original values of each indicator.

| | Yueyang | Hankou | Jiujiang | Chizhou | Mean |
|---|---|---|---|---|---|
| I1 | 33.04% | 13.37% | 25.56% | 9.62% | 20.40% |
| I2 | 34.14% | 9.67% | 17.45% | 4.58% | 16.46% |
| I3 | 100.00% | 100.00% | 100.00% | 100.00% | 100.00% |
| I4 | 90.00% | 54.55% | 90.91% | 50.00% | 71.36% |

The impact of each flood event and the performance for each reach in 2020 were evaluated. The daily water area during flood events was essential, but the SAR-derived result was not adequate. Therefore, the daily areas were computed using daily water level according to the coherence between the area and water level. Table 12 shows the flood severity indices of each reach in each event. Flood severity evaluation considered the flood duration in addition to the flood area, and the flood severity results were different from the water area changing process. The *FI*, *RP*, and *CFSI* are shown in Table 12.

**Table 12.** Final scores of each event or each reach.

| | Yueyang Reach | Hankou Reach | Jiujiang Reach | Chizhou Reach | FI | FI Rank |
|---|---|---|---|---|---|---|
| No.1 Flood | 0.44 | 0.30 | 0.41 | 0.28 | 1.43 | 3 |
| No.2 Flood | 0.47 | 0.36 | 0.46 | 0.34 | 1.63 | 1 |
| No.3 Flood | 0.49 | 0.36 | 0.44 | 0.33 | 1.62 | 2 |
| No.4 Flood | 0.40 | 0.21 | 0.37 | 0.19 | 1.17 | 4 |
| No.5 Flood | 0.41 | 0.20 | 0.36 | 0.18 | 1.15 | 5 |
| RP | 2.21 | 1.44 | 2.04 | 1.32 | -- | -- |
| RP Rank | 1 | 3 | 2 | 4 | -- | -- |
| CFSI | | 1.75 | | | -- | -- |

According to Table 12, the *CFSI* flood severity in 2020 was 1.75 times as much as that in 2019. The flood severity of each flood event can be analyzed from *FI*, and it can be concluded that: the impact of each flood event in 2020 is in order as follows: No.2 > No.3 > N0.1 > No.4 > No.5. Specifically, the flood severity indices are highest of each reach during the No.2 and the No.3 flood events, and little lower in No.1 flood event, although the No.1 flood event has the largest average daily rainfall and total rainfall. The flood severity indices for the No.4 flood event are close but slightly higher than those of the No.5 flood event.

The flood severity of each reach can be analyzed from *RP*. The following can be concluded: (1) According to *RP*, the four reaches are affected by the flood events in 2020 with the order as follows: Yueyang reach > Jiujiang reach > Hankou reach > Chizhou reach. The possible reason is that the impact of river-communicating lakes is greater than that of location and that the reaches in middle reach are more affected than that in lower reach in terms of location; (2) flood severity indexes are inconsistent with the spatial site: the flood severity index is higher in the Yueyang reach (in midstream) and the Jiujiang reach (in downstream) than that in the Hankou reach (in midstream) and the Chizhou reach (in downstream). A possible reason is that the Yueyang reach and Jiujiang reach serve as important mediums for the water exchange of the Yangtze River and the two river-communicating lakes, and the East Dongting Lake and Poyang Lake play an important role in flood storage throughout the flood season in 2020 and thus the frequent water circulation increased the flood severity in the two reaches.

### 3.3.2. Impact of Rainfall on Floods

The above section provides a detailed analysis of the changes in rainfall and water area during the 2020 Yangtze River flood events. The preliminary results indicate that the correlation between rainfall duration indicators, water area, and flood risk index is significantly higher than that of rainfall intensity indicators. Therefore, Figure 8 once again shows the line chart of changes in the three rainfall duration indicators, water area increases, and flood risk index among the five flood events. The graph reveals that among the rainfall duration indicators, the correlation between the 30-day cumulative rainfall and the water area increases, and the flood risk index is also at its highest. Table 13 shows the correlation between the increase in downstream and midstream water area to the flood risk index and the 30-day cumulative rainfall.

Based on the results of Table 13 and Figure 8, the impact of rainfall on the flood process can be summarized as follows: (1) From the intensity of rainfall, the downstream rainfall is more severe while from the cumulative rainfall and the midstream rainfall are more severe. The increase in water body area is more correlated with cumulative rainfall. This illustrates that water body area increase and precipitation are not synchronized and has a certain lag; (2) The correlation between flood risk index and cumulative rainfall is higher than that of water area increase. This finding suggests that adding a time dimension can more effectively reveal the severity of floods. Therefore, the method proposed in this paper proves to be effective in capturing and reflecting the severity of floods.

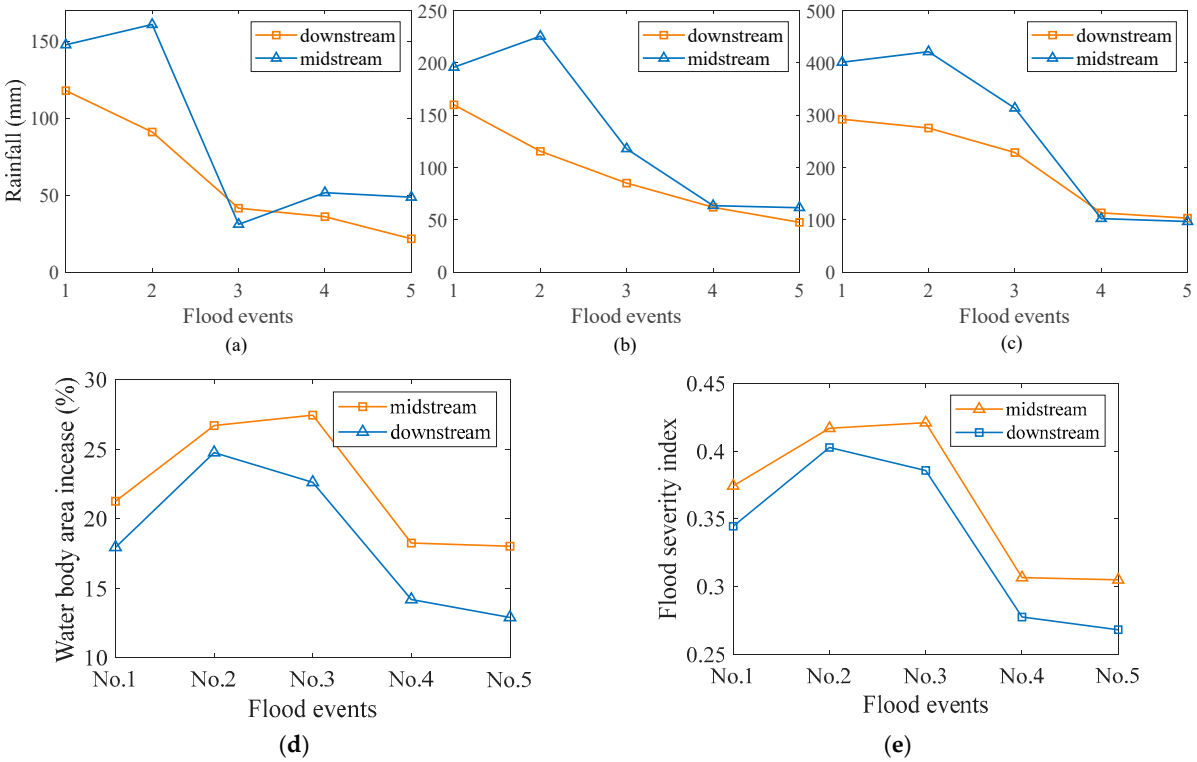


**Figure 8.** (**a**) The cumulative rainfall during 10 days before the flood event; (**b**) The cumulative rainfall for 15 days before the flood event; (**c**) The cumulative rainfall for 30 days before the flood event; (**d**) Water body area increases in each flood event in 2020 compared with that in 2019; (**e**) Flood severity index of each flood event in 2020.

**Table 13.** The R-square between cumulative rainfall for 30 days and water body area increase and flood severity index.

| | Water Body Area Increase | Flood Severity Index |
|---|---|---|
| Midstream | 0.51 | 0.72 |
| Downstream | 0.71 | 0.81 |

## 4. Discussion

A novel flood severity evaluation approach is proposed to numerically evaluate the flood process. This approach can be used to evaluate flood risk between any region of large hydrological systems or any flood event, regardless of their regional spatial differences and rainfall duration differences. To further elaborate on the significance of this research, the flood risk evaluation results by the novel approach (Table 12) are further compared to the traditional evaluation methods.

First, from the total rainfall of stations in the YRB, the severity of five flood events is No.1 > No.2 > No.5 > No.3 > No.4. This is inconsistent with the severity results of flood events by the novel approach (Table 12). The discrepancy arises because the duration of the flood is not considered, and more importantly, it overlooks the spatial distribution of rainfall, which plays a significant role in the flood severity.

Second, the rainfall was spatialized to a certain extent, the rainfall parameters of the midstream and downstream were counted, respectively (Figure 8). In Figure 8, the first three indicators are rainfall intensity indicators, and the last three indicators are regarded as rainfall duration indicators. The three rainfall intensity indicators show that the rainfall intensity of these five floods in the midstream and downstream is continuously decreasing. The rainfall duration indicators indicate that the cumulative rainfall of the No.2 flood is the most serious, similar to the No.1 flood. Combining these six indicators, the risk of the No.1 and No.2 flood is much higher than that of the latter three. This is inconsistent

with the severity results of flood events by the novel approach. Table 12 shows the No.2 flood event is the most serious, similar to the No.3. The reason for this is largely due to the spatial distribution of rainfall, and most importantly, to hydrological processes. We speculate that this difference is influenced by the impact of previous rainfall on hydrological conditions and water exchange between different regions. Rainfall does not equal surface water accumulation, and it will be redistributed on the surface due to hydrological activities. For large hydrological systems, the water body area is the ultimate state of flood.

Moreover, when the focus shifts from rainfall to water range, it is not essential to pay attention to the spatial distribution and duration of rainfall and surface hydrological activities. Any region and flood event can be chosen to do risk evaluation.

In addition, the following issues need to be discussed:

First, why has not multi-source satellite data been used to increase the frequency of water area monitoring. One reason for this is that SAR data are not affected by clouds and rain, while optical satellites are highly susceptible to these conditions, especially above the Yangtze River reach where clouds often appear during flood season. Another reason is that different satellites have varying widths and coverage ranges, and the coverage area of multiple satellites is relatively small, which does not meet the research objectives of this research. Therefore, this research only selected a single set of satellite data to obtain daily water body area and improve the temporal resolution of water area data through the correlation between water level and water area.

Second, the selection of the river reach plays a significant impact on the results. Changing the length or position of the river reach may affect the research results, which depends on the hydrological conditions of each river reach. The river reach of this study was determined based on the coverage area of Sentinel-1 imagery, and suitable study areas can be selected as needed in practical applications.

Third, water area was considered as the hydrological condition of the river reach in this research instead of the water volume. Hydrological or surveying, remote sensing, and other methods combined with river terrain data can estimate water volume, but it is more complex and requires more data compared to the water area extraction and does not meet the goal of rapid flood severity evaluation. The correlation between water area and water volume depends on the steepness of the river channel, which can be reflected to some extent by water level. The steeper the river channel, the faster the water level changes, and the gentler the river channel, the slower the water level changes. So, there is also a certain correlation between water area and water volume, but the specific impact needs further research, and the situation may be different for each river reach.

## 5. Conclusions

In this paper, Sentinel-1 data and the adaptive bimodal method are used to extract the temporal water body range to generate flood maps. A flood severity evaluation model based on daily water area is proposed, which considers both water area disparity and flood duration. This model can be applied to assess the flood risk between any region of large hydrological systems or any flood event, regardless of their regional spatial differences and rainfall duration differences. The correlation between flood risk index and cumulative rainfall indicates that adding a time dimension can more effectively reveal the severity of floods. The results can serve as a valuable reference for flood prevention and mitigation. The main conclusions can be summarized as follows:

(1) The average water body area in 2020 was 20.40% larger than that in 2019. The max water body area was 16.46% larger than that in 2019. The water body areas every day in 2020 were all greater than the average of 2019. 71.36% of days in 2020 were with an area greater than the maximum of 2019 compared to the total flood days in 2020.

(2) The flood severity evaluation results showed (a) the impact of each flood event in 2020 was in order as No.2 > No.3 > No.1 > No.4 > No.5. The continuous rainfall resulted in the most severe flooding during the No.2 and No.3 flood events. In future

flood prevention, each heavy rainfall should be dredged in time to prevent more serious consequences caused by continuous rainfall. (b) According to *RP*, the four reaches were affected by the flood events in 2020 in the order of Yueyang reach > Jiujiang reach > Hankou reach > Chizhou reach. A possible reason is that the impact of river-communicating lakes is greater than that of location, and the reaches in middle reach are more affected than that in lower reach in terms of location. In future flood prevention, the hydrological state of river-communicating lakes can be adjusted in time to prepare for the active response to floods. (c) The flood severity in 2020 was 1.75 times as much as that in 2019.

(3) The correlation between rainfall duration indicators, water area, and flood risk index is significantly higher than that of rainfall intensity indicators. Therefore, floods are more likely the result of cumulative rainfall.

**Author Contributions:** Conceptualization, M.H. and S.J.; methodology, M.H. and S.J.; software, M.H. and S.J.; validation, M.H. and S.J.; formal analysis, M.H.; investigation, M.H. and S.J.; resources, M.H. and S.J.; data curation, M.H. and S.J.; writing—original draft preparation, M.H. and S.J.; writing—review and editing, M.H., S.J. and Y.W.; visualization, Q.C.; supervision, Q.C.; project administration, M.H., Q.C. and Y.W.; funding acquisition, M.H., Q.C. and Y.W. All authors have read and agreed to the published version of the manuscript.

**Funding:** This research was funded by the Scientific Research Foundation of Education Department of Anhui Province of China, grant number 2023AH051633, the Chuzhou University Research and Development Fund for the Talent Startup Project, grant number 2023qd02, the Scientific Research Foundation of Education Department of Anhui Province of China, grant number 2023AH051592. National College Students' Innovation and Entrepreneurship Training Program of Chuzhou University in 2023, grant number 202310377007.

**Data Availability Statement:** Data are contained within the article.

**Acknowledgments:** The authors would like to acknowledge the data provided by the European Space Agency, Planet Labs, the Changjiang Maritime Safety Administration, the China Meteorological Data Service Center and National Aeronautics and Space Administration Goddard Earth Sciences Data and Information Services Center.

**Conflicts of Interest:** The authors declare no conflicts of interest.

## References

1. Hu, C.; Fang, C.; Cao, W. Shrinking of Dongting Lake and its weakening connection with the YZR: Analysis of the impact on flooding. *Int. J. Sediment Res.* **2015**, *30*, 256–262. https://doi.org/10.1016/j.ijsrc.2014.05.001.
2. Sun, R.; Gong, Z.; Gao, G.; Shah, A. Comparative analysis of Multi-Criteria Decision-Making methods for flood disaster risk in the Yangtze River Delta. *Int. J. Disaster Risk Reduct.* **2020**, *51*, 101768. https://doi.org/10.1016/j.ijdrr.2020.101768.
3. Xia, C.; Pahl-Wostl, C. Understanding the development of flood management in the middle YZR. *Environ. Innov. Soc. Transit.* **2012**, *5*, 60–75. https://doi.org/10.1016/j.eist.2012.10.001.
4. Black, A.; Burns, J.C. Re-assessing the flood risk in Scotland. *Sci. Total Environ.* **2002**, *294*, 169–184. https://doi.org/10.1016/S0048-9697(02)00062-1.
5. Rahmati, O.; Zeinivand, H.; Besharat, M. Flood hazard zoning in Yasooj region, Iran, using GIS and multi-criteria decision analysis. *Geomat. Nat. Hazards Risk* **2015**, *7*, 1000–1017. https://doi.org/10.1080/19475705.2015.1045043.
6. Pourghasemi, H.R.; Amiri, M.; Edalat, M.; Ahrari, A.H.; Lee, S. Assessment of Urban Infrastructures Exposed to Flood Using Susceptibility Map and Google Earth Engine. *IEEE J. Sel. Top. Appl. Earth Obs. Remote Sens.* **2021**, *14*, 1923–1937. https://doi.org/10.1109/JSTARS.2020.3045278.
7. Zhang, W.; Zhou, J.; Liu, Y.; Chen, X.; Wang, C. Emergency evacuation planning against dike-break flood: A GIS-based DSS for flood detention basin of Jingjiang in central China. *Nat. Hazards* **2021**, *81*, 1283–1301. https://doi.org/10.1007/s11069-015-2134-7.
8. Capolongo, D.; Refice, A.; Bocchiola, D.; D'Addabbo, A.; Vouvalidis, K.; Soncini, A.; Zingaro, M.; Bovenga, F.; Stamatopoulos, L. Coupling multitemporal remote sensing with geomorphology and hydrological modeling for post flood recovery in the Strymonas dammed river basin (Greece). *Sci. Total Environ.* **2019**, *651*, 1958–1968. https://doi.org/10.1016/j.scitotenv.2018.10.114.
9. Azimi, S.; Dariane, A.B.; Modanesi, S.; Bauer-Marschallinger, B.; Bindlish, R.; Wagner, W.; Massari, C. Assimilation of Sentinel 1 and SMAP—Based satellite soil moisture retrievals into SWAT hydrological model: The impact of satellite revisit time and product spatial resolution on flood simulations in small basins. *J. Hydrol.* **2020**, *581*, 124367. https://doi.org/10.1016/j.jhydrol.2019.124367.

10. Lu, C.; Zhou, J.; He, Z.; Yuan, S. Evaluating typical flood risks in Yangtze River Economic Belt: Application of a flood risk mapping framework. *Nat. Hazards* **2018**, *94*, 1187–1210. https://doi.org/10.1007/s11069-018-3466-x.
11. Jin, S.G.; Camps, A.; Jia, Y.; Wang, F.; Martin-Neira, M.; Huang, F.; Yan, Q.; Zhang, S.; Li, Z.; Edokossi, K.; et al. Remote sensing and its applications using GNSS reflected signals: Advances and prospects. *Satell. Navig.* **2024**, *5*, 19. https://doi.org/10.1186/s43020-024-00139-4.
12. Arvind, C.; Vanjare, A.; Omkar, S.; Senthilnath, J.; Mani, V.; Diwakar, P.G. Flood Assessment using Multi-temporal Modis Satellite Images. *Procedia Comput. Sci.* **2016**, *89*, 575–586. https://doi.org/10.1016/j.procs.2016.06.017.
13. Veh, G.; Korup, O.; Roessner, S.; Walz, A. Detecting Himalayan glacial lake outburst floods from Landsat time series. *Remote Sens. Environ.* **2018**, *207*, 84–97. https://doi.org/10.1016/j.rse.2017.12.025.
14. Volpi, M.; Petropoulos, G.; Kanevski, M. Flooding extent cartography with Landsat TM imagery and regularized kernel Fisher's discriminant analysis. *Comput. Geosci.* **2013**, *57*, 24–31. https://doi.org/10.1016/j.cageo.2013.03.009.
15. Tong, X.; Luo, X.; Liu, S.; Xie, H.; Chao, W.; Liu, S.; Liu, S.; Makhinov, A.N.; Makhinova, A.F.; Jiang, Y. An approach for flood monitoring by the combined use of Landsat 8 optical imagery and COSMO-SkyMed radar imagery. *ISPRS J. Photogramm.* **2018**, *136*, 144–153. https://doi.org/10.1016/j.isprsjprs.2017.11.006.
16. Goffi, A.; Stroppiana, D.; Brivio, P.A.; Bordogna, G.; Boschetti, M. Towards an automated approach to map flooded areas from Sentinel-2 MSI data and soft integration of water spectral features. *Int. J. Appl. Earth Obs.* **2020**, *84*, 101951. https://doi.org/10.1016/j.jag.2019.101951.
17. Grimaldi, S.; Xu, J.; Li, Y.; Pauwels, V.R.N.; Walker, J.P. Flood mapping under vegetation using single SAR acquisitions. *Remote Sens. Environ.* **2020**, *237*, 111582. https://doi.org/10.1016/j.rse.2019.111582.
18. Schlaffer, S.; Matgen, P.; Hollaus, M.; Wagner, W. Flood detection from multi-temporal SAR data using harmonic analysis and change detection. *Int. J. Appl. Earth Obs.* **2015**, *38*, 15–24. https://doi.org/10.1016/j.jag.2014.12.001.
19. Insom, P.; Cao, C.; Boonsrimuang, P.; Liu, D.; Saokarn, A.; Yomwan, P.; Xu, Y.F. A Support Vector Machine-Based Particle Filter Method for Improved Flooding Classification. *IEEE Geosci. Remote Sens.* **2015**, *12*, 1943–1947. https://doi.org/10.1109/LGRS.2015.2439575.
20. Huang, M.M.; Jin, S.G. Rapid Flood Mapping and Evaluation with a Supervised Classifier and Change Detection in Shouguang Using Sentinel-1 SAR and Sentinel-2 Optical Data. *Remote Sens.* **2020**, *12*, 2073. https://doi.org/10.3390/rs12132073.
21. Skakun, S. A Neural Network Approach to Flood Mapping Using Satellite Imagery. *Comput. Inform.* **2010**, *29*, 1013–1024. https://doi.org/10.1007/978-3-642-11840-1_26.
22. Liang, J.; Liu, D. A local thresholding approach to flood water delineation using Sentinel-1 SAR imagery. *ISPRS J. Photogramm.* **2020**, *159*, 53–62. https://doi.org/10.1016/j.isprsjprs.2019.10.017.
23. Li, Y.; Martinis, S.; Wieland, M. Urban flood mapping with an active self-learning convolutional neural network based on TerraSAR-X intensity and interferometric coherenc. *ISPRS J. Photogramm.* **2019**, *152*, 178–191. https://doi.org/10.1016/j.isprsjprs.2019.04.014.
24. Sandro, M.; André, T.; Stefan, V. Unsupervised Extraction of Flood-Induced Backscatter Changes in SAR Data Using Markov Image Modeling on Irregular Graphs. *IEEE Trans. Geosci. Remote Sens.* **2011**, *49*, 251–263. https://doi.org/10.1109/TGRS.2010.2052816.
25. Li, Y.; Martinis, S.; Plank, S.; Ludwig, R. An automatic change detection approach for rapid flood mapping in Sentinel-1 SAR data. *Int. J. Appl. Earth Obs.* **2018**, *73*, 123–135. https://doi.org/10.1016/j.jag.2018.05.023.
26. Long, S.; Fatoyinbo, T.; Policelli, F. Flood extent mapping for Namibia using change detection and thresholding with SAR. *Environ. Res. Lett.* **2014**, *9*, 035002. https://doi.org/10.1088/1748-9326/9/3/035002.
27. Shen, X.; Anagnostou, E.N.; Allen, G.H.; Brakenridge, G.R.; Kettner, A.J. Near-Real-Time non-obstructed flood inundation mapping using synthetic aperture radar. *Remote Sens. Environ.* **2019**, *221*, 302–315. https://doi.org/10.1016/j.rse.2018.11.008.
28. Liu, X.; Kettner, A.; Cheng, J.; Dai, S. Sediment characteristics of the Yangtze River during major flooding. *J. Hydrol.* **2020**, *590*, 125417. https://doi.org/10.1016/j.jhydrol.2020.125417.
29. Ezzine, A.; Darragi, F.; Rajhi, H.; Ghatassi, A. Evaluation of Sentinel-1 data for flood mapping in the upstream of Sidi Salem dam (Northern Tunisia). *Arab. J. Geosci.* **2018**, *11*, 170. https://doi.org/10.1007/s12517-018-3505-7.
30. Twele, A.; Cao, W.; Plank, S.; Martinis, S. Sentinel-1-based flood mapping: A fully automated processing chain. *Int. J. Remote Sens.* **2016**, *37*, 2990–3004. https://doi.org/10.1080/01431161.2016.1192304.
31. Carreño Conde, F.; De Mata Muñoz, M. Flood Monitoring Based on the Study of Sentinel-1 SAR Images: The Ebro River Case Study. *Water* **2019**, *11*, 2454. https://doi.org/10.3390/w11122454.
32. Liu, Q.; Huang, C.; Shi, Z.; Zhang, S. Probabilistic River Water Mapping from Landsat-8 Using the Support Vector Machine Method. *Remote Sens.* **2020**, *12*, 1374. https://doi.org/10.3390/rs12091374.

33. Kittipongvises, S.; Phetrak, A.; Rattanapun, P.; Brundiers, K.; Buizer, J.L.; Melnick, R. AHP-GIS analysis for flood hazard assessment of the communities nearby the world heritage site on Ayutthaya Island, Thailand. *Int. J. Disaster Risk Reduct.* **2020**, *48*, 101612. https://doi.org/10.1016/j.ijdrr.2020.101612.
34. Nachappa, T.G.; Piralilou, S.T.; Gholamnia, K.; Ghorbanzadeh, O.; Rahmati, O.; Blaschke, T. Flood susceptibility mapping with machine learning, multi-criteria decision analysis and ensemble using Dempster Shafer Theory. *J. Hydrol.* **2020**, *590*, 125275. https://doi.org/10.1016/j.jhydrol.2020.125275.